sensors

MDPI

Article

Highly Selective Gas Sensor Based on Litchi-like g-C_3N_4/In_2O_3 for Rapid Detection of H_2

Ji Zhang [1], Xu Li [2], Qinhe Pan [3], Tong Liu [4] and Qingji Wang [1,*]

[1] State Key Laboratory of Marine Resource Utilization in South China Sea, College of Information and Communication Engineering, Hainan University, Haikou 570228, China
[2] School of Chemical Engineering & Light Industry, Guangdong University of Technology, Guangzhou 510006, China
[3] School of Chemical Engineering and Technology, Hainan University, Haikou 570228, China
[4] School of Electronic and Information Engineering, Qingdao University, 308 Ningxia Street, Qingdao 266071, China
* Correspondence: wangqingji@hainanu.edu.cn

Abstract: Hydrogen (H_2) has gradually become a substitute for traditional energy, but its potential danger cannot be ignored. In this study, litchi-like g-C_3N_4/In_2O_3 composites were synthesized by a hydrothermal method and used to develop H_2 sensors. The morphology characteristics and chemical composition of the samples were characterized to analyze the gas-sensing properties. Meanwhile, a series of sensors were tested to evaluate the gas-sensing performance. Among these sensors, the sensor based on the 3 wt% g-C_3N_4/In_2O_3 (the mass ratio of g-C_3N_4 to In_2O_3 is 3:100) showeds good response properties to H_2, exhibiting fast response/recovery time and excellent selectivity to H_2. The improvement in the gas-sensing performance may be related to the special morphology, the oxygen state and the g-C_3N_4/In_2O_3 heterojunction. To sum up, a sensor based on 3 wt% g-C_3N_4/In_2O_3 exhibits preeminent performance for H_2 with high sensitivity, fast response, and excellent selectivity.

Keywords: g-C_3N_4/In_2O_3; litchi-like; H_2 sensor; fast response; high selectivity

Citation: Zhang, J.; Li, X.; Pan, Q.; Liu, T.; Wang, Q. Highly Selective Gas Sensor Based on Litchi-like g-C_3N_4/In_2O_3 for Rapid Detection of H_2. *Sensors* **2023**, *23*, 148. https://doi.org/10.3390/s23010148

Academic Editors: Vassilis Kodogiannis and Dedy Wijaya

Received: 24 November 2022
Revised: 12 December 2022
Accepted: 19 December 2022
Published: 23 December 2022

1. Introduction

Hydrogen (H_2) is a potential clean energy that has rich application prospects in automobile, aerospace, and other fields [1]. However, due to its flammable and explosive characteristics, H_2 can very easily cause disaster during utilization and storage [2]. Therefore, an effective survey of H_2 has become an important problem to be solved. At present, detection methods of H_2 include gas chromatography, mass spectrometry, gas sensors, and so on [3]. In the above methods, gas sensors have become the best choice, with the advantages of low cost, simple preparation, and small size [4]. Furthermore, the type of gas sensor include semiconductor oxide [5], catalytic combustion [6], solid electrolyte [7,8], etc. Among them, a semiconductor oxide sensor is widely used in people's lives because of the outstanding performance [9]. So far, many semiconductor oxides have been researched as sensing-materials in H_2 sensors, such as TiO_2, ZnO, SnO_2, NiO, and In_2O_3. Some reported H_2 sensors based on different semiconductor oxides are summarized in Table 1.

In_2O_3 is a common semiconductor with a band gap of 3.6 eV, which is broadly used in gas sensors [10]. Up to now, preparing In_2O_3 with distinct morphologies has proved to be an available measure to heighten the performance of gas sensors. However, a single In_2O_3-based sensor has the defects of low response and poor selectivity in practical applications [11]. Many researchers have made great efforts to enhance the gas-sensing performance, such as doping noble metals [12], fabricating heterojunctions [13], and constructing 2D materials or polymer composites [14,15]. Graphitic carbon nitride (g-C_3N_4) is a typical polymer semiconductor with a band gap of 2.76 eV, which has been used in

gas sensors owing to high chemical stability, large surface area, and good catalytic function [16,17]. It is reported that In_2O_3-based sensors can elevate gas-sensing performance through the g-C_3N_4 composite. Liu et al. prepared In_2O_3, and g-C_3N_4 was compounded by way of MOF, and the response value of the sensor achieved 294 to 100 ppm NO_x at RT [18]. Sun et al. synthesized g-C_3N_4/In_2O_3 through a calcination annealing process, and the response value of the sensor reached 1405 at 119 °C to 100 ppm formaldehyde [19]. The enhanced performance of the In_2O_3 sensor can be attributed to the formation of g-C_3N_4/In_2O_3 heterojunction different oxygen species content [20].

Table 1. Gas-sensing properties of H_2 sensor made by some semiconductor oxides.

Sensing Materials	Conc. (ppm)	Res.	$\tau_{res.}$ (s)	$\tau_{rec.}$ (s)	Ref.
WO_3-TiO_2	10000	5.62 [c]	48	5	[21]
Ag/ZnO	300	479% [b]	175	655	[22]
Pd/SnO_2	1000	1.2 [a]	214	51.5	[23]
Pt@NiO	5000	4.25 [c]	91	8	[24]
Pd-doped In_2O_3	100	3.6 [a]	4	7	[25]
3 wt% g-C_3N_4/In_2O_3	**100**	**180% [b]**	**2**	**2.4**	**This work**

Conc.: Concentration; Res.: Response; $\tau_{res.}$: Response time; $\tau_{rec.}$: Recovery time; Ref.: reference; [a] $R = R_a/R_g$; [b] $R = (R_a - R_g)/R_g \times 100\%$, [c] $R = R_g/R_a$.

In this paper, a litchi-like g-C_3N_4/In_2O_3 composite was successfully prepared by the hydrothermal method. Additionally, the morphology and composition of C_3N_4/In_2O_3 were characterized by XRD, SEM, TEM, and XPS. Sensors based on different amount of g-C_3N_4 composite were fabricated to investigate their gas-sensing specifics. Among them, the performance of the sensor based on 3 wt% g-C_3N_4/In_2O_3 was significantly improved for H_2, giving it the merits of a fast response and excellent selectivity.

2. Experiment

2.1. Synthesis of Peachcore-like Pure In_2O_3

All chemicals are purchased from Aladdin Reagent and are analytical grade without being further purified for use. In a typical process, 147.5 mg of $InCl_3 \cdot 4H_2O$ was dissolved in 15 mL of deionized water, then 15 mL of glycerol was added and stirred until it was homogeneous. Afterwards, 520 mg of $Na_3C_6H_5O_7 \cdot 2H_2O$ was added into the above solution and stirred vigorously for 20 min. Finally, 250 µL of NaOH (0.1 M) aqueous solution was added slowly to form a uniform solution. The obtained solution was transferred to an autoclave lined with 50 mL PTFE for a hydrothermal reaction at 190 °C for 16 h. After being cooled to room temperature, the precipitate was centrifuged with deionized water and absolute ethanol for several times. The powder was collected and dried at 80 °C overnight. The dried sample was placed in an Al_2O_3 boat and calcined in a muffle furnace at 400 °C for 2 h (2 °C/min) to obtain peachcore-like pure In_2O_3.

2.2. Synthesis of Litchi-like g-C_3N_4/In_2O_3

Firstly, 20 g of urea was added into a lidded crucible and heated in a muffle furnace at 550 °C for 2 h (2 °C/min) to prepare g-C_3N_4. Then, the prepared g-C_3N_4 was dispersed in 15 mL deionized water and sonicated for 2 h to ensure dispersion. Subsequently, 147.5 mg of $InCl_3 \cdot 4H_2O$ and 15 mL of glycerol was added the above solution in turn and stirred until homogeneous. Thereafter, 520 mg of $Na_3C_6H_5O_7 \cdot 2H_2O$ was added and stirred vigorously for 20 min. Finally, 250 µL of NaOH (0.1 M) aqueous solution was added to form a uniform solution. The subsequent process was the same as the preparation of pure In_2O_3. According to the different contents of g-C_3N_4, 1 wt% g-C_3N_4/In_2O_3, 3 wt% g-C_3N_4/In_2O_3, and 5 wt% g-C_3N_4/In_2O_3 composites were prepared, respectively.

2.3. Material Characterization

The crystal structures of as-samples were determined by an X-ray diffractometer (XRD, Rigaku Miniflex 600 X, Cu Kα1 radiation, λ = 1.5406 Å) operated at 40 kV and 15 mA. The morphology characteristics of samples were characterized by a scanning electron microscope (SEM, PHENOM SCIENTIFIC ProX G5, The Netherlands) and a transmission electron microscope (TEM, FEI Tecnai G2 F30, USA). X-ray photoelectron spectroscopy (XPS, Thermo escalab 250Xi, USA) was used for the chemical composition analysis of samples.

2.4. Fabrication and Measurement of Gas Sensors

The device structure of the gas sensor is shown in Figure 1. As-prepared samples were mixed with deionized water to form a uniform slurry and coated on an alumina ceramic tube as the sensing layer. The coated sensing layer was baked under an infrared lamp for 15 min. Then, the ceramic tube was calcined at 300 °C for 1 h (2 °C/min). Finally, the heating wire was passed through the ceramic tube and welded to a six-legged base to make a gas sensor. In addition, the components of the test gas are the target gas and the component gas, wherein the standard value of the target gas is 1% mol/mol and that of the component gas is nitrogen.

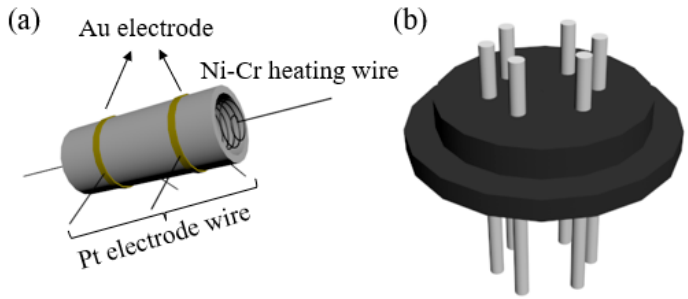

Figure 1. Sensor device structure (**a**) ceramic tube; (**b**) tube base.

The evaluation of gas-sensing performances was carried out in a static test system (50% RH, 25 °C), as shown in Figure 2. The heating current of the sensor was provided by the DC-regulated power supply, and the resistance value was recorded by the multimeter. The response value is defined as $R = (R_a - R_g)/R_g \times 100\%$, wherein R_a and R_g are the resistance value of the sensor respectively exposed to clean air and target gas. Additionally, the response/recovery time is defined as the time for 90% of the resistance change.

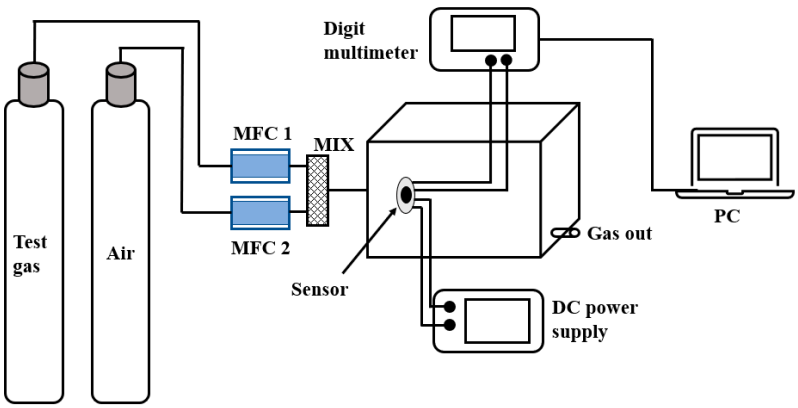

Figure 2. The gas-sensing test system.

3. Results and Discussion

3.1. Characterization of Material Structure

The crystal phase of the as-prepared samples was obtained by XRD, as shown in Figure 3. The g-C_3N_4 has two peaks at 2θ angles of 13.36° and 27.38°, which are related to the tris-triazine units and aromatic systems, respectively [26]. The diffraction peaks of pure In_2O_3 at 2θ angles of 22.37°, 30.99°, 32.61°, 45.61°, 50.25°, 57.20° and 58.19° are index to the crystal planes (012), (104), (110), (024), (116), (214) and (300) of In_2O_3 (JCPDS 22-0366). However, the diffraction peaks of g-C_3N_4 are not obviously observed in the XRD pictures of g-C_3N_4/In_2O_3 composites, probably due to the low content of g-C_3N_4 [27].

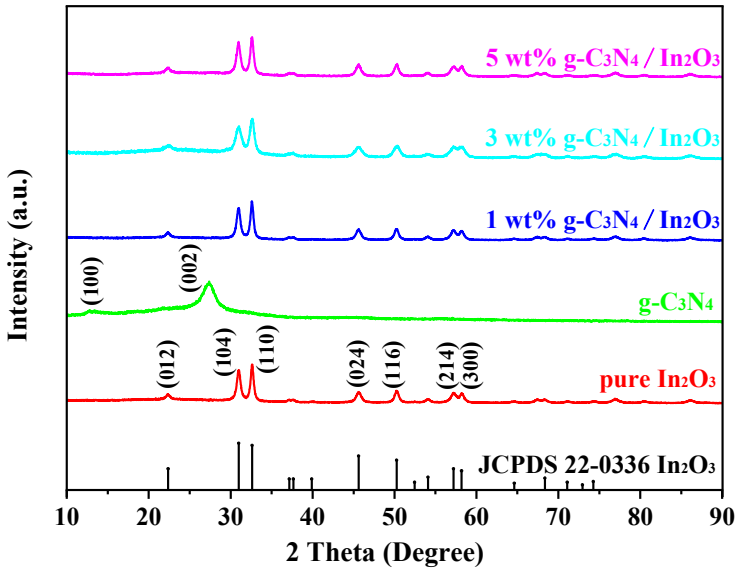

Figure 3. XRD patterns of as-prepared samples.

The SEM images of pure In_2O_3 and 3 wt% g-C_3N_4/In_2O_3 are shown in Figure 4. Pure In_2O_3 exhibits a peachcore-like structure with a diameter of about 250 nm in Figure 4a,b. The morphology of 3 wt% g-C_3N_4/In_2O_3 possesses a distinctive litchi-like structure, and the diameter of 3 wt% g-C_3N_4/In_2O_3 is only 130 nm, as shown in Figure 4c,d. Apparently, the morphology of In_2O_3 was changed from peachcore-like to litchi-like, and the diameter of 3 wt% g-C_3N_4/In_2O_3 is smaller about 100 nm than that of pure In_2O_3. Moreover, the size of 3 wt% g-C_3N_4/In_2O_3 is more uniform than that of pure In_2O_3. The crystallite sizes of as-prepared samples were calculated by the Scherrer formula:

$$D = \frac{K\lambda}{\beta cos\theta} \quad (1)$$

where K is Scherrer constant of 0.9, λ is the X-ray wavelength of 0.15406 nm, β is the half-width of the diffraction peak, and θ is the Bragg diffraction angle. The average size of pure In_2O_3, 1 wt% g-C_3N_4/In_2O_3, 3 wt% g-C_3N_4/In_2O_3, and 3 wt% g-C_3N_4/In_2O_3 is about 15 nm, 14.4 nm, 13.9 nm and 12.6 nm, respectively. Based on the above results, it is inferred that the g-C_3N_4 may inhibit the growth of In_2O_3 crystal, thus leading to morphological changes [28].

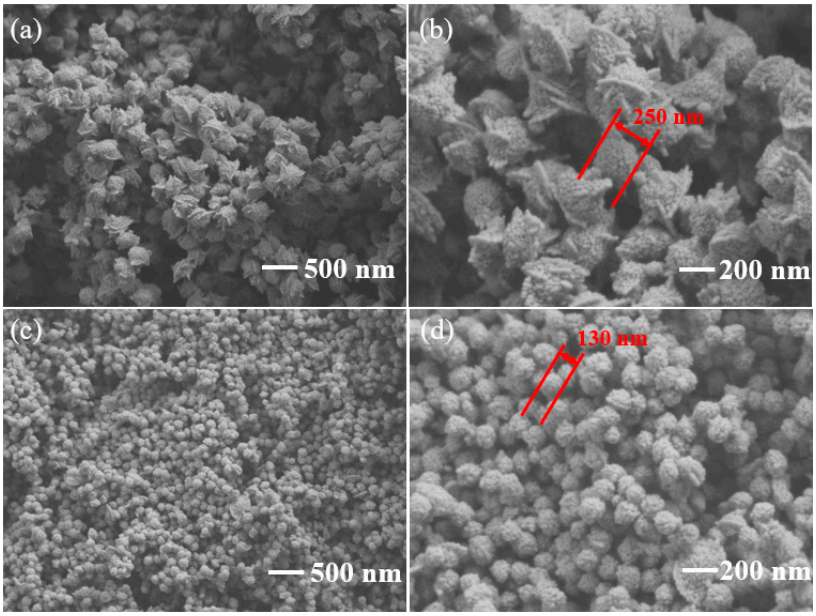

Figure 4. SEM images of (**a**,**b**) pure In_2O_3; (**c**,**d**) 3 wt% g-C_3N_4/In_2O_3.

The microstructure of 3 wt% g-C_3N_4/In_2O_3 was characterized by TEM and HRTEM, as shown in Figure 5. Through TEM in Figure 5a, we can clearly see that the 3 wt% g-C_3N_4/In_2O_3 presents a litchi-like structure with uniform size. Furthermore, HRTEM in Figure 5b is manifested by the different lattice spacings of In_2O_3, which plainly indicates In_2O_3 with a highly crystalline form. The three lattice spacings are 0.12 nm, 0.18 nm and 0.17 nm, which are assigned to the (012), (110) and (104) planes of In_2O_3, respectively. In addition, the element mapping is shown in Figure 5c–h. From element mapping, it can be explicitly noticed that the In, O, C, and N elements are evenly distributed; this can be evidence that the 3 wt% g-C_3N_4/In_2O_3 composite was successfully prepared.

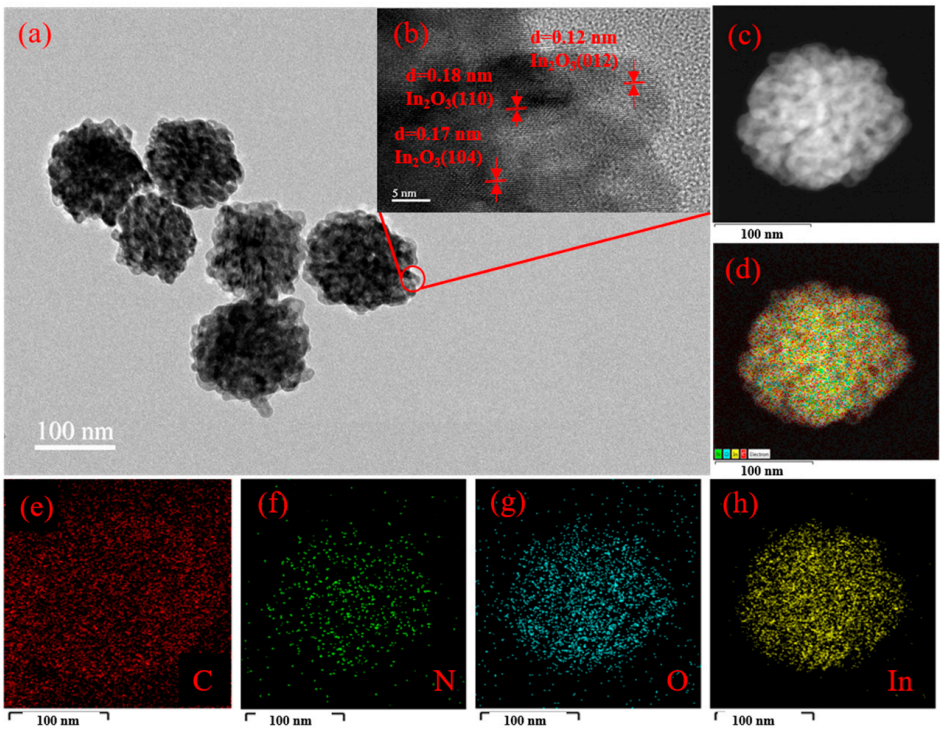

Figure 5. 3 wt% g-C_3N_4/In_2O_3 (**a**) TEM image; (**b**) HRTEM; (**c**–**h**) elemental mapping.

To analyze the chemical composition of pure In_2O_3 and 3 wt% g-C_3N_4/In_2O_3, the XPS is shown in Figure 6. As shown in Figure 6a, the In 3d of pure In_2O_3 and 3 wt% g-C_3N_4/In_2O_3 have two strong peaks at 451.6 eV, 444.1 eV and 451.7 eV, 444.2 eV, which correspond to In $3d_{5/2}$ and In $3d_{3/2}$, respectively [29]. The O 1s peak spectrums in Figure 6b are decomposed into three fitting peaks around 532.1 eV, 531.2 eV, 529.5 eV and 532.2 eV, 531.2 eV, 529.6 eV, wherein the fitting peaks are assigned to the hydroxyl (OH) or chemisorbed oxygen (O_C), oxygen vacancy (O_V), and lattice oxygen (O_L) [30,31]. Furthermore, the O_C, O_V, and O_L content of pure In_2O_3 and 3 wt% g-C_3N_4/In_2O_3 are about 8.56%, 23.59%, 67.85% and 9.14%, 33.42%, 57.44%, respectively. It is worth noting that the content of O_C and O_V increases with the introduction of g-C_3N_4. It may be one of the reasons why the gas-sensing performance of 3wt% g-C_3N_4/In_2O_3-based sensors has improved [32,33]. The C 1s spectrum displays three peaks at 288.3 eV, 286.3 eV, and 284.8 eV, as shown in Figure 6c. These three peaks of C 1s respectively belong to the sp^{2-} bonded carbon (N–C=N) and the sp^{3-} fitted carbon bond from surface defects of g-C_3N_4 and carbon atoms (C-C) [34]. However, the N 1s peak appears to be a weak peak at 398.8eV, as shown in Figure 6d, which may be caused by the low content of g-C_3N_4 [35].

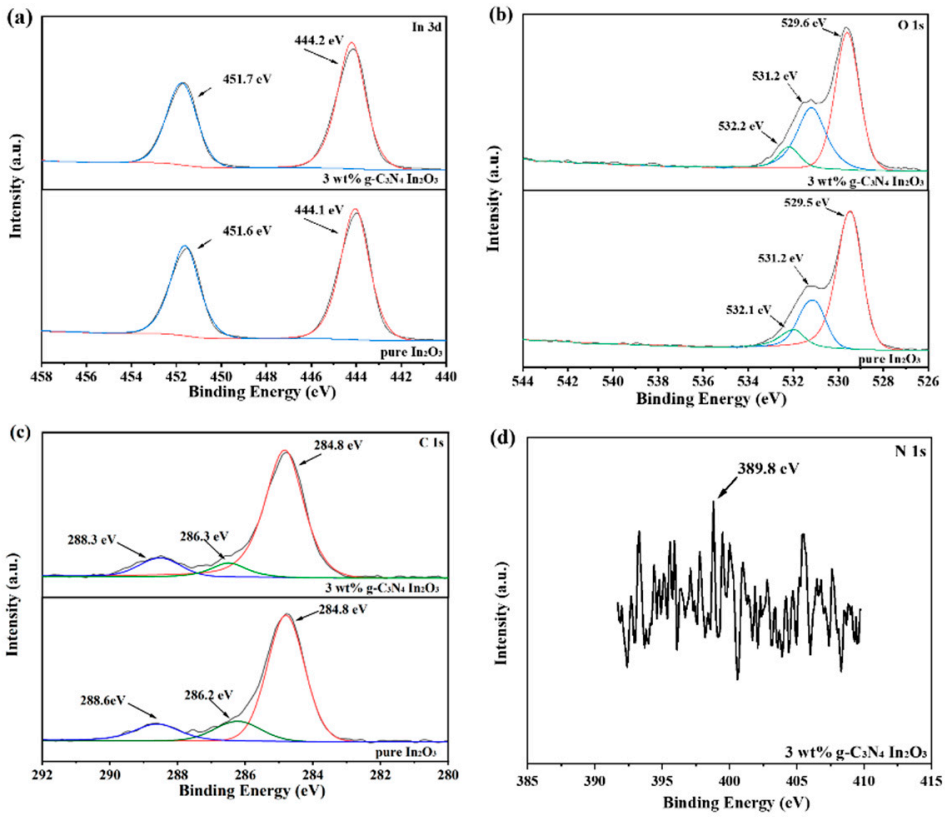

Figure 6. XPS spectra of as-prepared samples (**a**) In 3d; (**b**) O 1s; (**c**) C 1s; (**d**) N 1s.

3.2. Gas-Sensing Properties

To determine the optimal operating temperature of the sensors, the different sensors based on g-C_3N_4/In_2O_3 composites with different proportions were evaluated from 225 °C to 300 °C, as shown in Figure 7. When the operating temperature reaches 275 °C, the response value is 180% to 100 ppm H_2 of 3 wt% g-C_3N_4/In_2O_3 sensor in Figure 7a, which is 3.5 times that of pure In_2O_3 sensor. The operating temperature can be explained according to the desorption equilibrium of the gas molecules and the chemical reaction kinetics. When the working temperature is too low, the gas molecules do not have enough heat energy and kinetic energy to react on the In_2O_3 surface, so the adsorption capacity of the gas is reduced. However, when the operating temperature is too high, the gas molecules adsorbed on the In_2O_3 surface will have a high activity and escape before the electron carrier transfer,

resulting in a reduced response [3,36]. In addition, the response values of different sensors were tested with different concentrations of H_2 (10~1000 ppm) at 275 °C. As exhibited in Figure 7b, the response value of the 3 wt% g-C_3N_4/In_2O_3 sensor is greatly improved compared with other sensors within the whole range of H_2 concentrations. With the increase in the H_2 concentration, the rising trend of the response value curve is gradually stable, which may indicate that the sensor is gradually saturated.

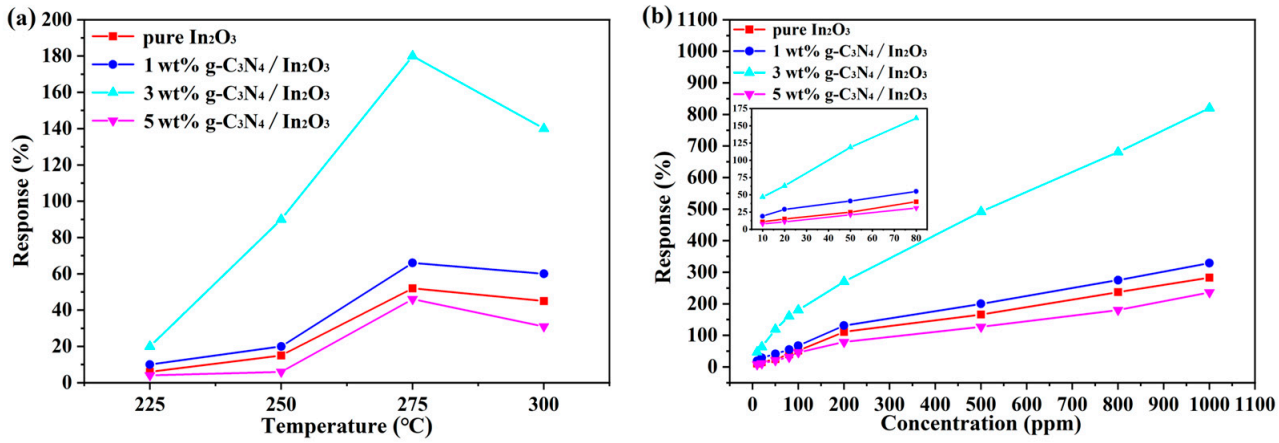

Figure 7. (**a**) Response values of sensors vs. operating temperatures to 100 ppm H_2; (**b**) response values of sensors vs. different concentrations H_2 at 275 °C.

The response/recovery time of the different sensors at 275 °C is shown in Figure 8a–d. It is not hard to notice that the increase of g-C_3N_4 content, which may have a positive action in the sensor. Although g-C_3N_4 is beneficial to the response and recovery characteristics of the sensor, excessive g-C_3N_4 may play a reverse role. Furthermore, the 3 wt% g-C_3N_4/In_2O_3 sensor exhibits fast response/recovery time (2 s/2.4 s) to 100 ppm H_2. From Figure 8e, even if it is in a high concentration H_2 atmosphere, the 3 wt% g-C_3N_4/In_2O_3 sensor also demonstrated extremely fast response/recovery time. The above results reveal that the 3 wt% g-C_3N_4/In_2O_3 sensor has great potential in practical application. The R_a of different sensors at different temperatures are shown in Figure 8f; the R_a decrease with the increase in temperature. In addition, the R_a of sensors based on g-C_3N_4/In_2O_3 is lower than that of the pure In_2O_3 and decreased with the increasing amount of g-C_3N_4 in the composites. The reason for the increase in conductivity is firstly due to the increase in oxygen vacancy in g-C_3N_4/In_2O_3. The second reason is attributed to the C–N bond breaking, which releases a lot of electrons [37]. Based on the above reasons, it can be proven that the sensor based on g-C_3N_4/In_2O_3 has high conductivity.

Stability and reproducibility are important indicators of a sensor's performance, and the evaluation result of the 3 wt% g-C_3N_4/In_2O_3 sensor at 275 °C is shown in Figure 9. As shown in Figure 9a, the dynamic curves of the 3 wt% g-C_3N_4/In_2O_3 sensor is exhibited. Within the variation range of H_2 concentrations, the response and recovery characteristics of the 3 wt% g-C_3N_4/In_2O_3 sensor are stable. Meanwhile, the detection limit was tested to 1 ppm H_2, and the response value is 10%. Reproducibility was evaluated by continuous exposure to 50 ppm H_2 for five cycles, as shown in Figure 9b. In the five-cycle experiment, the response/recovery time and response value were basically stable without significant change. By assessing the gas-sensing properties of the 3 wt% g-C_3N_4/In_2O_3 sensor, it was sufficienly proven that the sensor has fine stability and reproducibility.

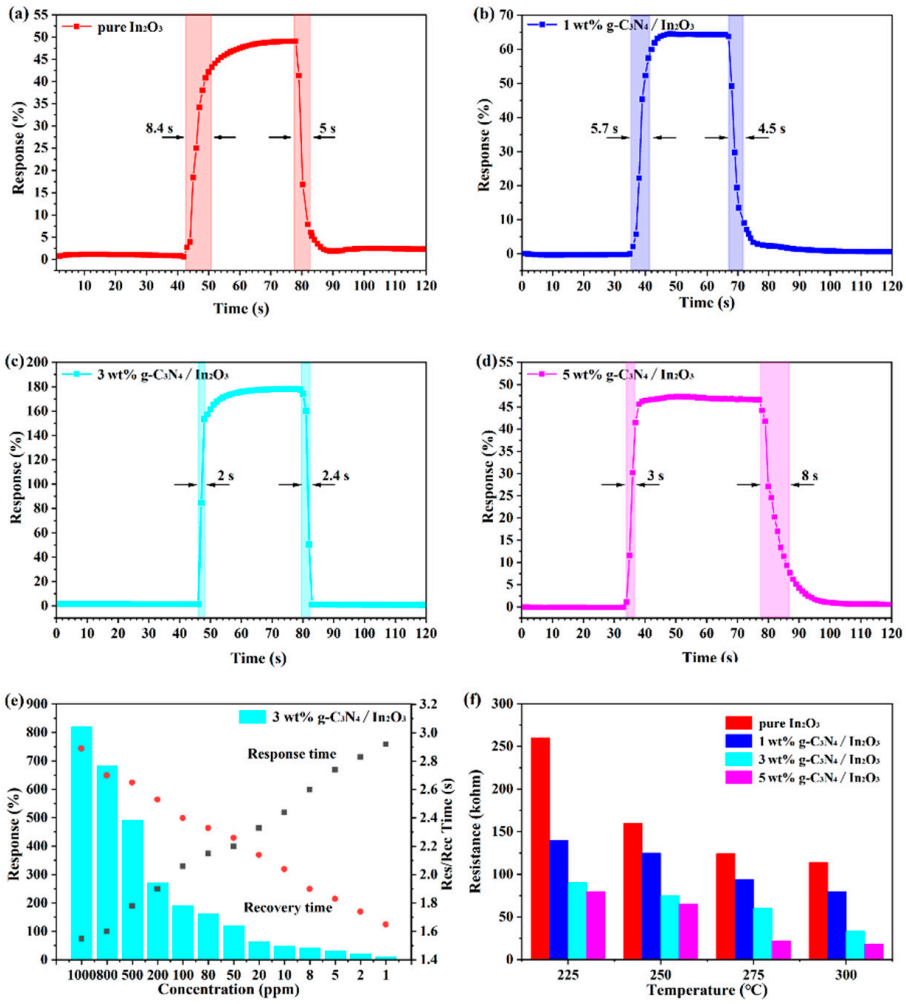

Figure 8. (**a**–**d**) Response/recovery time of different sensors; (**e**) response/recovery time of 3 wt% g-C_3N_4/In_2O_3 to different concentrations of H_2 at 275 °C; (**f**) R_a at different temperatures of different sensors.

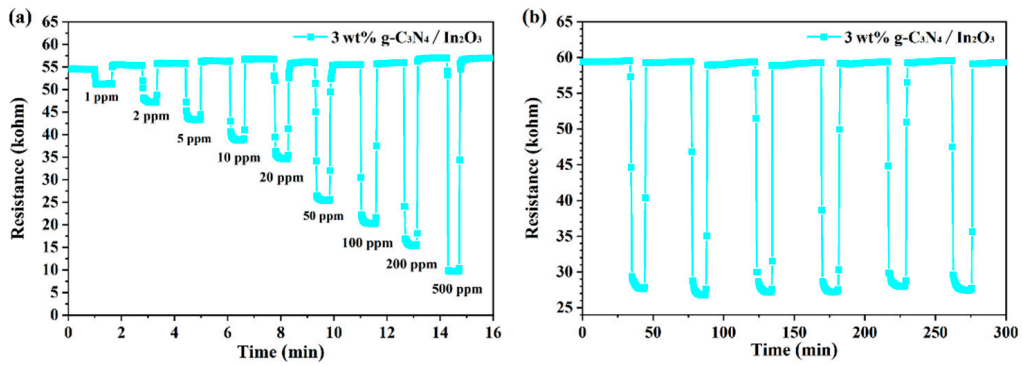

Figure 9. (**a**) Dynamic response curve of sensor to different concentrations of H_2 at 275 °C; (**b**) the five-cycle response/recovery curve of the sensor to 50 ppm H_2 at 275 °C.

Selectivity is a momentous parameter for the practical application of the sensor. Various gases were tested at 275 °C for the appraisement of different sensors, as presented in Figure 10. Among them, 1 wt% g-C_3N_4/In_2O_3 and 3 wt% g-C_3N_4/In_2O_3 sensors exhibit similar selectivity characteristics, which possess a higher response value to 50 ppm H_2 than other gases (50 ppm SO_2, 50 ppm NH_3, 50 ppm CO_2, 50 ppm CO, 50 ppm CH_4, 100 ppm NO_2). Besides, the response value of the 3 wt% g-C_3N_4/In_2O_3 sensor is three times that of

the 1 wt% g-C_3N_4/In_2O_3 sensor to 50 ppm H_2. Meanwhile, the response value of the 3 wt% g-C_3N_4/In_2O_3 sensor to 50 ppm H_2 is 7.5 times that of 50 ppm SO_2 (the secondary response gas). As we all know, CO, CH_4, and H_2 are common fuel gases, and the response values of the 3 wt% g-C_3N_4/In_2O_3 sensor to H_2 are 20 times and 40 times that of CO and CH_4 of 50 ppm, respectively. The improvement of H_2 selectivity is due to the better dispersion of litchi-like 3wt% g-C_3N_4/In_2O_3 compared with pure In_2O_3, which makes H_2 with the smallest molecular size easy to diffuse [38]. In addition, at 275 °C for the sensor based on the 3 wt% g-C_3N_4/In_2O_3 surface, the adsorption energy of H_2 gas is much higher than that of other gases [22]. From the above results, the 3 wt% g-C_3N_4/In_2O_3 sensor exhibits excellent selectivity in H_2 detection.

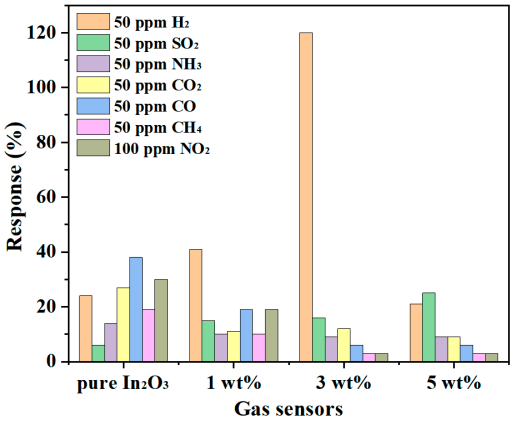

Figure 10. Gas selectivity of different sensors at 275 °C.

The long-term stability is shown in Figure 11, which was evaluated by continuous exposure to 50 ppm H_2 at 275 °C within 2 weeks. It is distinctly perceived from Figure 11a that the response value to 50 ppm H_2 is not significantly changed. Moreover, the transient curves for different days are shown in Figure 11b–d, and it is noteworthy that the air resistance (R_a) and response features of the sensor are basically stable. In view of the above assessment, it can be assured that the 3 wt% g-C_3N_4/In_2O_3 sensor has good long-term stability for H_2 detection.

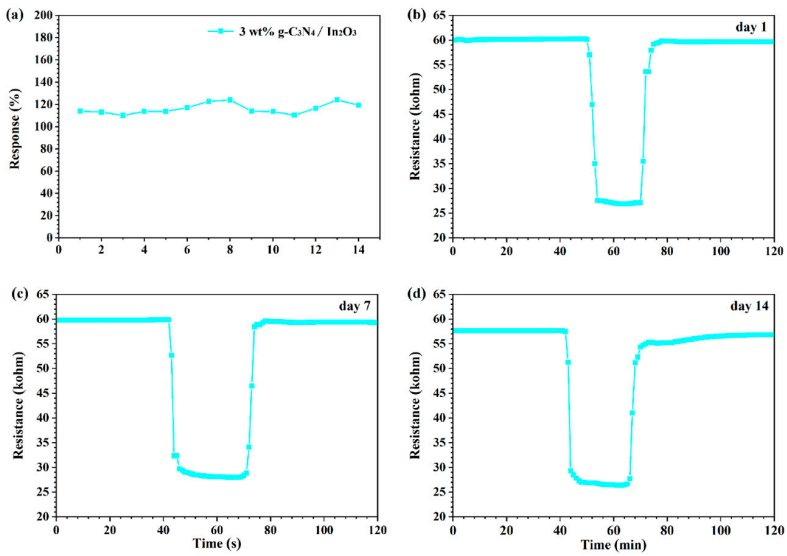

Figure 11. (**a**) Long-term stability over 2 weeks for the sensor to 50 ppm H_2 at 275 °C; (**b**–**d**) transient curve of different days.

3.3. Gas Sensing Mechanism

In order to understand the enhanced properties of the H_2 sensor based on g-C_3N_4/In_2O_3, the gas-sensing mechanism of the In_2O_3 sensor was analyzed. In air at different temperatures, the oxygen molecules on the surface of In_2O_3 materials will become O_2^- (<147 °C), O^- (147 °C–397 °C), O^{2-} (>397 °C), as follows in Equations (2)–(5) [29].

$$O_2 \rightarrow O_{2(ads)} \tag{2}$$

$$O_{2(ads)} + e^- \rightarrow O_2{}^-{}_{(ads)} \tag{3}$$

$$O_2{}^-{}_{(ads)} + e^- \rightarrow 2O^-{}_{(ads)} \tag{4}$$

$$O^-{}_{(ads)} + e^- \rightarrow O^{2-}{}_{(ads)} \tag{5}$$

$$2\,H + O^-{}_{(ads)} \rightarrow H_2O + e^- \tag{6}$$

In this paper, the optimum operating temperature was determined to be 275°C, so most of the oxygen molecules are converted into O^-. When the In_2O_3 sensor exposure to H_2, the H molecules are oxidized by O^- to form H_2O and free electrons as in Equation (6) [22]. The reaction process is shown in Figure 12a. The elevated gas-sensing performance of sensor based on 3 wt% g-C_3N_4/In_2O_3 may be attributed to the morphology characteristic, the oxygen state and the g-C_3N_4/In_2O_3 heterojunctions. The first reason is the distinctive litchi-like morphology of 3 wt% g-C_3N_4/In_2O_3. Through observing SEM and TEM photos, the 3 wt% g-C_3N_4/In_2O_3 has smaller size and better dispersion than pure In_2O_3. The performance of the sensor based on 3 wt% g-C_3N_4/In_2O_3 may be improved due to the unique morphology configuration.

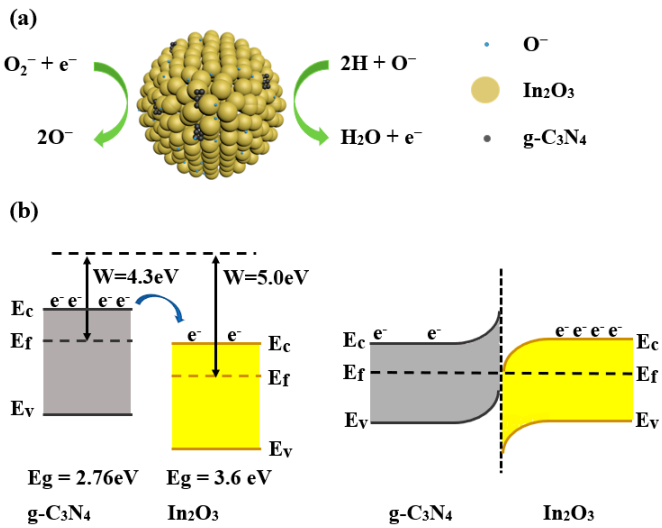

Figure 12. (**a**) Sketch map of gas-sensing mechanism; (**b**) energy band diagram of In_2O_3 and g-C_3N_4.

The second reason can be attributed to the adjustment of the oxygen state. The XPS results show that the O_V and O_C contents in 3 wt% g-C_3N_4/In_2O_3 are higher than pure in In_2O_3. For the sensor based on 3 wt% g-C_3N_4/In_2O_3, a large amount of O_V provides more active sites for the adsorption of active oxygen, and the increase in O_C content indicates that more chemically adsorbed oxygen participates in the redox reaction [19]. Therefore the performance of the 3 wt% g-C_3N_4/In_2O_3 sensor may be improved. The last reason is the formation of the g-C_3N_4/In_2O_3 heterojunction [19]. The work functions and band gaps of g-C_3N_4 and In_2O_3 are W = 4.3 [39], E_g = 2.76 eV [16] and W = 5.0 [13], E_g = 3.6 eV [10], respectively, as exhibited in Figure 12b. The electrons flow from g-C_3N_4 to In_2O_3 to the new equilibrium of the Fermi level. Therefore, the sensor based on 3 wt% g-C_3N_4/In_2O_3 shows excellent response characteristics [40].

4. Conclusions

In this work, the g-C_3N_4/In_2O_3 composite was prepared by a hydrothermal method. The morphology features and chemical compositions of g-C_3N_4/In_2O_3 were characterized by XRD, SEM, TEM and XPS. The sensor based on 3 wt% g-C_3N_4/In_2O_3 perform excellent gas-sensing behavior. The response value of 3 wt% g-C_3N_4/In_2O_3 was 180% to 100 ppm H_2 at 275 °C, which is 3.5 times higher than that of the pure In_2O_3 sensor. Furthermore, the 3 wt% g-C_3N_4/In_2O_3 sensor exhibits fast response/recovery time (2 s/2.4 s) to 100 ppm H_2 and excellent selectivity ($R_{50\ ppm\ H2}/R_{50\ ppm\ CH4}$ = 40, $R_{50\ ppm\ H2}/R_{50\ ppm\ CO}$ = 20). The improvement of sensor performance based on 3 wt% g-C_3N_4/In_2O_3 can be attributed to the special morphology characteristic, the state of oxygen, and the g-C_3N_4/In_2O_3 heterojunctions. In conclusion, this work provides a useful composite for preparing highly efficient H_2 sensors and proves that this composite has certain application value.

Author Contributions: Writing—Original draft, J.Z.; writing—Review, X.L.; resources Q.P.; writing—Editing, T.L.; conceptualization and supervision, Q.W. All authors have read and agreed to the published version of the manuscript.

Funding: This study is supported by the National Nature Science Foundation of China (61803172), Hainan Provincial Natural Science Foundation of China (621RC509) and the Start-Up Research Foundation of Hainan University (KYQD(ZR)1910).

Institutional Review Board Statement: Not applicable.

Informed Consent Statement: Not applicable.

Data Availability Statement: The data of this study can be obtained from the corresponding authors.

Conflicts of Interest: The authors declare no conflict of interest.

References

1. Liang, J.-Y.; Chou, Y.-J.; Yin, C.-W.; Lin, W.-C.; Lin, H.-J.; Chen, P.-W.; Tseng, Y.-C. Realization of an H_2/CO dual-gas sensor using CoPd magnetic structures. *Appl. Phys. Lett.* **2018**, *113*, 182401. [CrossRef]
2. Constantinoiu, I.; Viespe, C. Development of Pd/TiO_2 Porous Layers by Pulsed Laser Deposition for Surface Acoustic Wave H_2 Gas Sensor. *Nanomaterials* **2020**, *10*, 760. [CrossRef]
3. Meng, X.; Bi, M.; Xiao, Q.; Gao, W. Ultrasensitive gas sensor based on Pd/SnS_2/SnO_2 nanocomposites for rapid detection of H_2. *Sens. Actuators B Chem.* **2022**, *359*, 131612. [CrossRef]
4. Kumaresan, M.; Venkatachalam, M.; Saroja, M.; Gowthaman, P. TiO_2 nanofibers decorated with monodispersed WO_3 heterostructure sensors for high gas sensing performance towards H_2 gas. *Inorg. Chem. Commun.* **2021**, *129*, 108663. [CrossRef]
5. Wang, Y.; Bao, L.; Cao, Z.; Li, C.; Li, X.; Liu, F.; Sun, P.; Lu, G. Microwave-assisted hydrothermal synthesis of Pt/SnO_2 gas sensor for CO detection. *Chin. Chem. Lett.* **2020**, *31*, 2029–2032. [CrossRef]
6. Wang, Y.; Tong, M.M.; Zhang, D.; Gao, Z. Improving the Performance of Catalytic Combustion Type Methane Gas Sensors Using Nanostructure Elements Doped with Rare Earth Cocatalysts. *Sensors* **2010**, *11*, 19–31. [CrossRef]
7. Cao, Z.; Gao, Q.; Zhou, M.; Li, X.; Wang, Q. $LaNiTiO_3$-SE-based stabilized zirconium oxide mixed potentiometric SO_2 gas sensor. *Ceram. Int.* **2021**, *48*, 9269–9276. [CrossRef]
8. Islam, S.; Bhardwaj, A.; Mathur, L.; Kim, I.-H.; Park, J.-Y.; Song, S.-J. Effects of electrolyte variation on ammonia sensing temperature for $BiVO_4$ sensing electrode in mixed potential gas sensor. *Sens. Actuators B Chem.* **2022**, *371*, 132504. [CrossRef]
9. Wang, Q.; Liu, F.; Lin, J.; Lu, G. Gas-sensing properties of In-Sn oxides composites synthesized by hydrothermal method. *Sens. Actuators B Chem.* **2016**, *234*, 130–136. [CrossRef]
10. Guo, S.-Q.; Zhang, X.; Hao, Z.-W.; Gao, G.-D.; Li, G.; Liu, L. In_2O_3 cubes: Synthesis, characterization and photocatalytic properties. *RSC Adv.* **2014**, *4*, 31353–31361. [CrossRef]
11. Hu, J.; Sun, Y.; Xue, Y.; Zhang, M.; Li, P.; Lian, K.; Zhuiykov, S.; Zhang, W.; Chen, Y. Highly sensitive and ultra-fast gas sensor based on CeO_2-loaded In_2O_3 hollow spheres for ppb-level hydrogen detection. *Sens. Actuators B Chem.* **2018**, *257*, 124–135. [CrossRef]
12. Liu, W.; Xie, Y.; Chen, T.; Lu, Q.; Ur Rehman, S.; Zhu, L. Rationally designed mesoporous In_2O_3 nanofibers functionalized Pt catalysts for high-performance acetone gas sensors. *Sens. Actuators B Chem.* **2019**, *298*, 126871. [CrossRef]
13. Zhang, K.; Qin, S.; Tang, P.; Feng, Y.; Li, D. Ultra-sensitive ethanol gas sensors based on nanosheet-assembled hierarchical ZnO-In_2O_3 heterostructures. *J. Hazard. Mater.* **2020**, *391*, 122191. [CrossRef] [PubMed]
14. Hussain, C.M.; Thomas, S. *Handbook of Polymer and Ceramic Nanotechnology*; Springer: Berlin/Heidelberg, Germany, 2019.
15. Achary, L.S.K.; Kumar, A.; Barik, B.; Nayak, P.S.; Tripathy, N.; Kar, J.P.; Dash, P. Reduced graphene oxide-$CuFe_2O_4$ nanocomposite: A highly sensitive room temperature NH_3 gas sensor. *Sens. Actuators B Chem.* **2018**, *272*, 100–109. [CrossRef]

16. Hou, M.; Gao, J.; Yang, L.; Guo, S.; Hu, T.; Li, Y. Room temperature gas sensing under UV light irradiation for $Ti_3C_2T_x$ MXene derived lamellar TiO_2-C/g-C_3N_4 composites. *Appl. Surf. Sci.* **2021**, *535*, 147666. [CrossRef]
17. Maji, B.; Achary, L.S.K.; Barik, B.; Jyotsna Sahoo, S.; Mohanty, A.; Dash, P. $MnCo_2O_4$ decorated (2D/2D) rGO/g-C_3N_4-based Non-Enzymatic sensor for highly selective and sensitive detection of Chlorpyrifos in water and food samples. *J. Electroanal. Chem.* **2022**, *909*, 116115. [CrossRef]
18. Liu, Y.; Liu, J.; Pan, Q.; Pan, K.; Zhang, G. Metal-organic framework (MOF) derived In_2O_3 and g-C_3N_4 composite for superior NO_x gas-sensing performance at room temperature. *Sens. Actuators B Chem.* **2021**, *352*, 131001. [CrossRef]
19. Sun, D.; Wang, W.; Zhang, N.; Liu, C.; Li, X.; Zhou, J.; Ruan, S. G-C3N4/In_2O_3 composite for effective formaldehyde detection. *Sens. Actuators B Chem.* **2022**, *358*, 131414. [CrossRef]
20. Ullah, M.; Lv, H.; Liu, Z.; Bai, X.; Chen, J.; Zhang, Y.; Wang, J.; Sun, B.; Li, L.; Shi, K. Rational fabrication of a g-C_3N_4/NiO hierarchical nanocomposite with a large surface area for the effective detection of NO_2 gas at room temperature. *Appl. Surf. Sci.* **2021**, *550*, 149368. [CrossRef]
21. Li, H.; Wu, C.-H.; Liu, Y.-C.; Yuan, S.-H.; Chiang, Z.-X.; Zhang, S.; Wu, R.-J. Mesoporous WO_3-TiO_2 heterojunction for a hydrogen gas sensor. *Sens. Actuators B Chem.* **2021**, *341*, 130035. [CrossRef]
22. Agarwal, S.; Kumar, S.; Agrawal, H.; Moinuddin, M.G.; Kumar, M.; Sharma, S.K.; Awasthi, K. An efficient hydrogen gas sensor based on hierarchical Ag/ZnO hollow microstructures. *Sens. Actuators B Chem.* **2021**, *346*, 130510. [CrossRef]
23. Kadhim, I.H.; Abu Hassan, H.; Abdullah, Q.N. Hydrogen Gas Sensor Based on Nanocrystalline SnO_2 Thin Film Grown on Bare Si Substrates. *Nano-Micro Lett.* **2016**, *8*, 20–28. [CrossRef]
24. Wu, C.-H.; Zhu, Z.; Chang, H.-M.; Jiang, Z.-X.; Hsieh, C.-Y.; Wu, R.-J. Pt@NiO core–shell nanostructure for a hydrogen gas sensor. *J. Alloys Compd.* **2020**, *814*, 151815. [CrossRef]
25. Chen, L.; He, X.; Liang, Y.; Sun, Y.; Zhao, Z.; Hu, J. Synthesis and gas sensing properties of palladium-doped indium oxide microstructures for enhanced hydrogen detection. *J. Mater. Sci. Mater. Electron.* **2016**, *27*, 11331–11338. [CrossRef]
26. Yan, S.C.; Li, Z.S.; Zou, Z.G. Photodegradation performance of g-C_3N_4 fabricated by directly heating melamine. *Langmuir* **2009**, *25*, 10397–10401. [CrossRef]
27. Akhtar, A.; Jiao, C.; Chu, X.; Liang, S.; Dong, Y.; He, L. Acetone sensing properties of the g–C_3N_4–CuO nanocomposites prepared by hydrothermal method. *Mater. Chem. Phys.* **2021**, *265*, 124375. [CrossRef]
28. Zhang, Y.; Liu, J.; Chu, X.; Liang, S.; Kong, L. Preparation of g–C_3N_4–SnO_2 composites for application as acetic acid sensor. *J. Alloys Compd.* **2020**, *832*, 153355. [CrossRef]
29. Li, S.; Xie, L.; He, M.; Hu, X.; Luo, G.; Chen, C.; Zhu, Z. Metal-Organic frameworks-derived bamboo-like CuO/In_2O_3 Heterostructure for high-performance H_2S gas sensor with Low operating temperature. *Sens. Actuators B Chem.* **2020**, *310*, 127828. [CrossRef]
30. Ma, J.; Fan, H.; Zheng, X.; Wang, H.; Zhao, N.; Zhang, M.; Yadav, A.K.; Wang, W.; Dong, W.; Wang, S. Facile metal-organic frameworks-templated fabrication of hollow indium oxide microstructures for chlorine detection at low temperature. *J. Hazard. Mater.* **2020**, *387*, 122017. [CrossRef]
31. Pasupuleti, K.S.; Reddeppa, M.; Chougule, S.; Bak, N.-H.; Nam, D.-J.; Jung, N.; Cho, H.D.; Kim, S.-G.; Kim, M.-D. High performance langasite based SAW NO_2 gas sensor using 2D g-C_3N_4@TiO_2 hybrid nanocomposite. *J. Hazard. Mater.* **2022**, *427*, 128174. [CrossRef]
32. Zhu, Z.; Liu, C.; Jiang, F.; Liu, J.; Liu, G.; Ma, X.; Liu, P.; Huang, R.; Xu, J.; Wang, L. Flexible fiber-shaped hydrogen gas sensor via coupling palladium with conductive polymer gel fiber. *J. Hazard. Mater.* **2021**, *411*, 125008. [CrossRef]
33. Han, D.; Zhai, L.; Gu, F.; Wang, Z. Highly sensitive NO_2 gas sensor of ppb-level detection based on In_2O_3 nanobricks at low temperature. *Sens. Actuators B Chem.* **2018**, *262*, 655–663. [CrossRef]
34. Cao, S.W.; Liu, X.F.; Yuan, Y.P.; Zhang, Z.Y.; Liao, Y.S.; Fang, J.; Loo, S.C.J.; Sum, T.C.; Xue, C. Solar-to-fuels conversion over In_2O_3/g-C_3N_4 hybrid photocatalysts. *Appl. Catal. B—Environ.* **2014**, *147*, 940–946. [CrossRef]
35. Li, X.; Li, Y.; Sun, G.; Luo, N.; Zhang, B.; Zhang, Z. Synthesis of a Flower-Like g-C_3N_4/ZnO Hierarchical Structure with Improved CH4 Sensing Properties. *Nanomaterials* **2019**, *9*, 724. [CrossRef] [PubMed]
36. Walker, J.M.; Akbar, S.A.; Morris, P.A. Synergistic effects in gas sensing semiconducting oxide nano-heterostructures: A review. *Sens. Actuators B Chem.* **2019**, *286*, 624–640. [CrossRef]
37. Zhao, Y.; Wang, X.; Wang, T.; Li, X.; Fu, Y.; Zhao, G.; Xu, X. g-C_3N_4 templated synthesis of 3DOM SnO_2/CN enriched with oxygen vacancies for superior NO_2 gas sensing. *Appl. Surf. Sci.* **2022**, *604*, 154618. [CrossRef]
38. Xie, F.; Li, W.; Zhang, Q.; Zhang, S. Highly Sensitive and Selective CO/NO/H_2/NO_2 Gas Sensors Using Noble Metal (Pt, Pd) Decorated MO_x (M = Sn, W) Combined With SiO_2 Membrane. *IEEE Sens. J.* **2019**, *19*, 10674–10679. [CrossRef]
39. Guo, W.W.; Huang, L.L.; Zhang, J.; He, Y.Z.; Zeng, W. Ni-doped SnO_2/g-C_3N_4 nanocomposite with enhanced gas sensing performance for the eff;ective detection of acetone in diabetes diagnosis. *Sens. Actuator B Chem.* **2021**, *334*, 11. [CrossRef]
40. Patrick, D.S.; Govind, A.; Bharathi, P.; Mohan, M.K.; Harish, S.; Archana, J.; Navaneethan, M. Hierarchical ZnO/g-C_3N_4 nanocomposites for enhanced NO_2 gas sensing applications. *Appl. Surf. Sci.* **2023**, *609*, 155337. [CrossRef]